Check for updates

A novel automated morphological analysis of Iba1+ microglia using a deep learning assisted model

Lucas Stetzik[1]*, Gabriela Mercado[1], Lindsey Smith[2],
Sonia George[1], Emmanuel Quansah[1], Katarzyna Luda[3],
Emily Schulz[1], Lindsay Meyerdirk[1], Allison Lindquist[1],
Alexis Bergsma[4], Russell G. Jones[3], Lena Brundin[1],
Michael X. Henderson[1], John Andrew Pospisilik[4] and
Patrik Brundin[1]

[1]Parkinson's Disease Center, Department of Neurodegenerative Science, Van Andel Institute, Grand Rapids, MI, United States, [2]Aiforia Inc, Cambridge Innovation Center, Cambridge, MA, United States, [3]Department of Metabolism and Nutritional Programming, Van Andel Institute, Grand Rapids, MI, United States, [4]Department of Epigenetics, Van Andel Institute, Grand Rapids, MI, United States

There is growing evidence for the key role of microglial functional state in brain pathophysiology. Consequently, there is a need for efficient automated methods to measure the morphological changes distinctive of microglia functional states in research settings. Currently, many commonly used automated methods can be subject to sample representation bias, time consuming imaging, specific hardware requirements and difficulty in maintaining an accurate comparison across research environments. To overcome these issues, we use commercially available deep learning tools Aiforia® Cloud (Aifoira Inc., Cambridge, MA, United States) to quantify microglial morphology and cell counts from histopathological slides of Iba1 stained tissue sections. We provide evidence for the effective application of this method across a range of independently collected datasets in mouse models of viral infection and Parkinson's disease. Additionally, we provide a comprehensive workflow with training details and annotation strategies by feature layer that can be used as a guide to generate new models. In addition, all models described in this work are available within the Aiforia® platform for study-specific adaptation and validation.

KEYWORDS

deep learning, microglia, Parkinson's disease, viral infection, olfactory dysfunction, synuclein

---

Abbreviations: Iba1, ionized calcium-binding adaptor protein-1; PFF, oreformed fibrils; αSyn, alpha synuclein.

Introduction

Microglia are resident CNS macrophages with a reactive functional state induced by injury as well as several proinflammatory conditions and are involved in the pathogenesis of diverse neurodegenerative conditions. Change in microglial reactivity, or "microgliosis," is characterized by microglia proliferation, as well as transcriptional and morphological changes (Colton and Wilcock, 2010; Parakalan et al., 2012; Walker and Lue, 2015; Awogbindin et al., 2020). Morphological change in particular, which ranges from highly ramified to an ameboid cell shape, has been widely used to measure change in microglial functional state and its involvement in different pathological conditions, including mouse models of neurodegenerative diseases, traumatic brain injury and infections, among others (Davis et al., 1994; Nakajima and Kohsaka, 2001; Zusso et al., 2012).

The study of neurodegenerative diseases and neuroinflammation often requires accurate and reproducible image analysis of histological slides. Ionized calcium-binding adaptor protein-1 (Iba1) is a cytoskeletal protein specific to microglia and macrophages commonly used in histological analysis and can be used to quantify microglia phenotype (Ito et al., 1998; Ohsawa et al., 2000; Shi et al., 2020; Lier et al., 2021; Schwabenland et al., 2021). Immunolabeling of Iba1 in the cytoskeleton of microglia allows for quantification of changes in morphology, specifically calculation of a cell's area to perimeter ratio, which increases as microglia become more ameboid (Kongsui et al., 2015; Kolosowska et al., 2020; Johnson et al., 2021). Currently, quantification of the area/perimeter ratio is achieved using ImageJ or FIJI software, sometimes with the Sholl analysis plugin (Ferreira et al., 2014; Clarke et al., 2021). Other automated and semiautomated methods often require custom designed software or scripts that can be challenging to apply across research environments (Heindl et al., 2018; George et al., 2019; Gober et al., 2022). However, many of these methods require manual cell imaging at high magnifications on bright field or confocal microscopes, which can increase the duration of time needed to complete a full analysis and potentially introduce a sampling bias. Recently, some researchers have developed accurate, effective deep learning tools to overcome these limitations, but implementing these tools across research environments can be a challenge to investigators without access to method-specific hardware and formal computer science training (Kyriazis et al., 2019; Bascuñana et al., 2020; Leyh et al., 2021). By using commercially available deep learning tools (Aiforia®) to develop and validate a microglia morphology model, we have been able to establish a workflow for results with fewer limitations in application and reproducibility.

In this report, we provide an automated model capable of detecting microglia and change in their reactivity with accuracy comparable to expert human histopathology. We compare our area/perimeter results with our previously described semiautomated MATLAB script and demonstrate that by using the method described here, this model can be generalized or adapted to specific datasets across research environments. Additionally, we present an effective comparison of analysis results from independently collected datasets, related to viral infection. Finally, we provide a clear example of how the accuracy and sampling power of our method could translate to reduced variability for datasets with lower sample sizes, in a mouse model of Parkinson's disease. Taken together, the work presented here provides a user-friendly option for quantifying microglia morphology, and more broadly an exciting advancement in access to flexible machine learning technology capable of quantifying imaging features.

Materials and methods

To produce a robust generalizable method for quantifying microglia morphology using commercially available deep learning tools, we utilized tissue samples from six independent studies across 3 labs in 2 departments at the Van Andel Institute (Grand Rapids, MI, United States). While these labs use many of the same general practices regarding animal treatment, tissue collection and tissue processing, some of these practices vary slightly across labs. Subtle methodological variability, such as a slightly different background signal for Iba1, is potentially important for demonstrating how generalizable this method of artificial intelligence (AI) model development can be across different research environments. Please see the section "Author contributions" for a description of each lab/researcher's involvement.

Animals

We utilized 7- to 8-week-old wild type (WT) C57BL/6J mice for the model of α-synuclein (αSyn) induced olfactory dysfunction; 20- to 22-week-old WT C57BL/6N mice for the model of viral infection; 10- to 12-week-old C57BL/6J and NSG mice for the adaptive transfer dataset (George et al., 2021); 20- to 22-week-old wild typeTrim28 heterozygous mice on a FVBN background (Whitelaw et al., 2010) for the model of striatal αSyn aggregation. All animals were bred in the vivarium at Van Andel Institute. Mice were housed at a maximum of 4 per cage under a 12-hour light-/dark cycle with *ad libitum* access to water and food. The housing of the animals and all procedures were carried out in accordance with the Guide for the Care and Use of Laboratory Animals (United States National Institutes of Health) and were approved by Van Andel Institute's Institutional Animal Care and Use Committee.

Viral infection model

C57BL/6N wild-type male mice 20-22 weeks of age were injected intraperitoneal with 2×10^5 PFU/mouse of lymphocytic choriomeningitis virus acute (LCMV, Armstrong strain) produced and titrated as previously described (Battegay et al., 1991; Welsh and Seedhom, 2008). LCMV has been previously shown to induce change in microglia reactivity (Zhou et al., 2008). Seven days after injections, animals were euthanized and brains were collected.

PFF seeding αSyn aggregation mouse models

αSyn induced olfactory dysfunction

Mouse αSyn aggregates were produced as previously described (Volpicelli-Daley et al., 2014) and kindly provided by Dr. Kelvin Luk (University of Pennsylvania Perelman School of Medicine, United States). Before surgery, αSyn preformed fibrils (PFFs) were sonicated in a water-bath cup-horn sonicator for 4 min (QSonica, Q700 sonicator, 50% power, 120 pulses at 1s ON, 1s OFF) and maintained at room temperature until injection. For control injections, αSyn monomeric protein was maintained on ice until intracerebral injections were performed. Mice were anesthetized with isoflurane and injected unilaterally in the right olfactory bulb (OB) (coordinates from bregma: AP: +5.4 mm; ML: –0.75 mm and DV: –1.0 mm from dura) with 0.8 μL of PFFs or monomeric αSyn (5 μg/μL) for the αSyn induced olfactory dysfunction model and the monomer model respectively; and with matching volumes of vehicle phosphate buffered saline (PBS) as control. Injections were made at a rate of 0.2 μL/min using a glass capillary attached to a 10 μL Hamilton syringe. After injection, the capillary was left in place for five min before being slowly removed. Prior to incision, the animals were injected with local anesthetic into the site of the future wound margin (0.03 mL of 0.5% Ropivacaine; Henry Schein, United States). Following surgery mice received 0.5 mL saline s.c. for hydration, and 0.04 mL Buprenex (Henry Schein) s.c. for analgesia. Mice injected with αSyn into the olfactory system were euthanized 8–15 weeks after surgery.

Striatal αSyn aggregation

Stereotactic injections were performed unilaterally into the dorsal striatum (coordinates from bregma: AP: +0.2 mm; ML: ±2.0 mm and DV: –2.6 mm from dura). Experimental animals were injected with 1 μL of mouse PFFs (1 μg/μL) and control animals were injected with 1 μL of vehicle phosphate buffered saline (PBS) at 20–22 weeks of age. Tissue was collected when animals reached 36 weeks of age. Mice were anesthetized by intraperitoneal IP injection with tribromoethanol (Avertin) and perfused transcardially with 0.9% saline, followed by 4% PFA in phosphate buffer. Brains were harvested, post-fixed for 24 h in 4% PFA at 4C, and cryoprotected in 30% sucrose in phosphate buffer for at least 3 days at 4°C or until taken for sectioning. The entire brain of each mouse was cut into 40 μm free-floating coronal sections on a freezing microtome and stored in a cryoprotectant solution consisting of 30% sucrose and 30% ethylene glycol in PBS at –20°C until immunostaining. For detection of the antibody with DAB, we utilized a peroxidase-based method (Vectastain ABC kit and DAB kit; Vector laboratories). Stained sections were mounted onto gelatin-coated glass slides, dehydrated, and coverslipped with Cytoseal 60 mounting medium (Thermo Fisher Scientific).

Immunohistochemical analysis

Animals were anesthetized with sodium pentobarbital (130 mg/kg; Sigma Aldrich) for tissue collection at the indicated time points. Brains were isolated after transcardial perfusion with saline and fixation with 4% PFA. After dissection, brains were post fixed overnight with 4% PFA and then stored at 4°C in 30% sucrose in PBS until sectioning. Brains were frozen and coronal sections of 40 μm were cut on a sliding microtome (Leica, Germany) and collected as serial tissue sections spaced by 240 μm. For DAB immunoprecipitation and antigen detection we used a standard peroxidase-based method using a series of free-floating coronal sections (every 6th section). Samples were blocked with 10% normal goat serum, 0.4% BSA and 0.1% Triton-X100 in PBS for 2 h after which they were incubated with primary antibody directed against Iba1 at 1:1,000 (Wako, 019-19741) at RT overnight. On the following day, samples were triple washed with 0.1% Triton-X100 in PBS and incubated with biotinylated anti-rabbit antibody (Vector Laboratories, BA-1000) for 2 h at room temperature, triple washed again with the same solution and treated with Vectastain ABC kit (Vector Laboratories, PK-4000). Antigen detection was performed with Vector DAB (Vector Laboratories, SK-4100). After mounting and dehydration, slides were coverslipped with Cytoseal 60 mounting medium (Thermo Fisher Scientific).

Microglia morphology quantifications using MATLAB

Mouse coronal tissue sections were viewed under an Eclipse Ni-U microscope (Nikon); images were captured with a color Retiga Exi digital CCD camera (QImaging) using NIS Elements AR 4.00.08 software (Nikon). Microglia hydraulic radius (area/perimeter ratio) was determined as previously described (George et al., 2019). In short, color (RBG) images were generated using a 60x oil objective. Following imaging, a custom segmentation MATLAB (R2019b, The MathWorks, Natick, MA, United States) script assessed the morphology of the imaged microglia, using user defined microglia identification

and a pixel-based quantification of the area and the perimeter. These values were then converted to micrometers and used to determine their area/perimeter ratio in MS Excel v16.41.

Microglia morphology quantifications using Aiforia®

Image acquisition

Z-stacks of mounted Iba1-stained tissue sections were captured at 20x magnification using a whole slide scanner (Zeiss, Axioscan Z1) at a 0.22 μm/pixel resolution. Extended depth focus (EDF) was used to collapse the z-stacks into 2D images as they were collected. Tissue thickness was set to 20 μm, z-stacks were collected at 3 μm intervals and the method setting selected was *Contrast*. The images were exported with 85% compression as.jpeg files. The digitized images were then uploaded Aiforia® image processing and management platform (Aiforia Inc, Cambridge, MA, United States) for analysis with deep learning convolutional neural networks (CNNs) and supervised learning.

Assessment of microglia morphology using Aiforia®

A supervised, multi-layered CNN was trained using scans of coronal mouse brain tissue sections stained for Iba1, to recognize Iba1+ microglia in mice. The AI model was trained on the most diverse and representative images from across multiple Iba1 datasets and was adapted to each dataset to create multiple AI models capable of accurately detecting Iba1-stained microglia collected by multiple investigators. Whole slide images were loaded to the Aiforia® cloud for the training data, and each feature layer was trained using tools in the Aiforia® Cloud platform. All analysis results, including the location of each microglia cell, were determined using the automated deep learning algorithm developed using Aiforia®. However, the analysis regions (i.e., brain regions; striatum, motor cortex, etc.) were annotated manually.

Training details and annotation strategies by feature layer

The first feature layer ("tissue") was annotated using semantic segmentation to distinguish between Iba1+ tissue and glass slide background. The training regions for the "parent" tissue layer can be described using three tissue training region annotation strategies: positive tissue signal, background, and positive-signal/background interface (edge of tissue). Each training image included at minimum 2 positive tissue signal, 3 background, and 1 positive-signal/background interface training regions. The tissue layer was trained at 10,000 iterations, CNN complexity set to *Very Complex*, and 100 μm field of view.

Object detection was used for the "child" feature layer ("microglia") to identify Iba1+ microglia and overall cell

diameter. Cell diameters were binned by 10 μm intervals ranging from 10 to 110 μm. Additionally, segmentation was used to distinguish each cell from the surrounding background tissue. On average, 9.5 instance segmentation annotations were included per training image. The training regions for the microglia layer can also be described using four microglia training region annotation strategies: small training regions annotating 2–4 cells, extended background, cell-background, and broad area of interest (Table 1).

Small training regions were primarily used in the early stages of model development, and each image included 1.5 small training regions on average. Cell selection for the small annotations was pseudo counter-balanced across images to include examples of microglia from the olfactory bulb, piriform cortex, anterior olfactory nucleus, dorsal striatum, and substantia nigra. A preliminary model was trained using 1,500 training iterations, and subsequent analyses were performed for 10 of the 35 training images to qualitatively assess model performance. Model performance evaluation was then used to streamline the inclusion of additional annotations, most specifically the broad area of interest training regions.

Broad area of interest training regions were annotated using the Aiforia® Converter Tool to convert correct AI model predictions that resulted from the previous AI model training round into training annotations for the subsequent round of training. Using this technique, we quickly amplified the number of annotations across a multitude of ROIs that captured staining and scanning variability within the datasets. To maintain a consistent definition for microglia detection, each object converted from analysis results was reviewed and, if necessary, manually adjusted for object diameter and position centering. These annotations made up most of the examples needed for robust microglia identification by supplying 30–800 microglia training examples per training region and, on average, 0.8 broad area of interest training regions were included per training image.

Extended background training region annotations typically included 2–4 cells and extracellular background that extended or "branched" across most of the tissue section in 2–3 directions without including cell bodies or processes. Each branch ranged from 1 to 4 mm, approximately. The aim of the "branching" annotations was to reduce the occurrence of false positives by providing adequate examples of background tissue. On average, 3.6 extended background training regions were included per training image. Finally, to eliminate the occurrence of false positives that result from the incorrect identification of a single microglia as two or more objects, training regions were carefully drawn/edited to exclude any overlapping portions of the object annotations (see Table 1 example images). The final version of this microglia layer completed after 11,789 training iterations, with pre-training instance segmentation network complexity set to *ultra complex,* and post-training object detection *gain* and *Level of detail* adjusted to optimize model performance (object

TABLE 1 Annotation strategies.
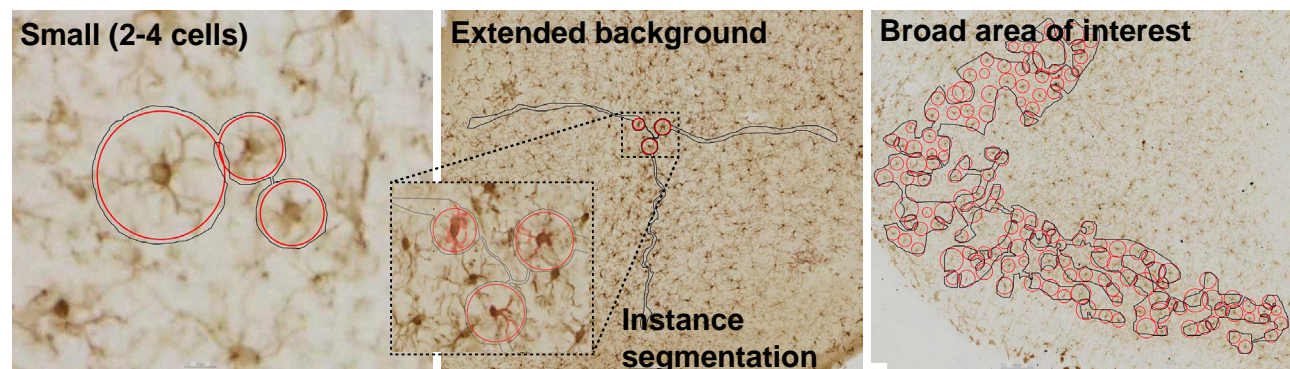
Model	# of object annotations	Small (2-4 cells)	Broad area of interest	Extended background	Instance segmentation	cell background
α Syn induced olfactory dysfunction	4187	51	27	126	334	0
Viral infection	745	635	0	3	136	278
Striatal α Syn aggregation	997	0	18	0	18	0

Model specific annotations used to produce validated deep learning models. (*Example images*) Solid black lines designate the training regions, red circles (object annotations) used to identify microglia, and red outline surrounding microglia (insert) designates instance segmentation annotation. Annotation strategies: Small (2–4 cells), Extended background, and Broad area of interest (*as described* in section "Details of model adaptation across independently collected Iba1+ datasets"*)* (Model) identifies which of the microglia models the table details pertain to: αSyn induced olfactory dysfunction, Viral infection, Striatal αSyn aggregation. (Remaining columns: # of object annotations – cell background) Each column represents one annotation strategy and the number of annotations for each annotation strategy.

detection gain 2.1, instance segmentation gain 4, and level of detail "*High*") (**Supplementary Figure 1A**).

Comparison of microglia morphology assessment methods across brain regions
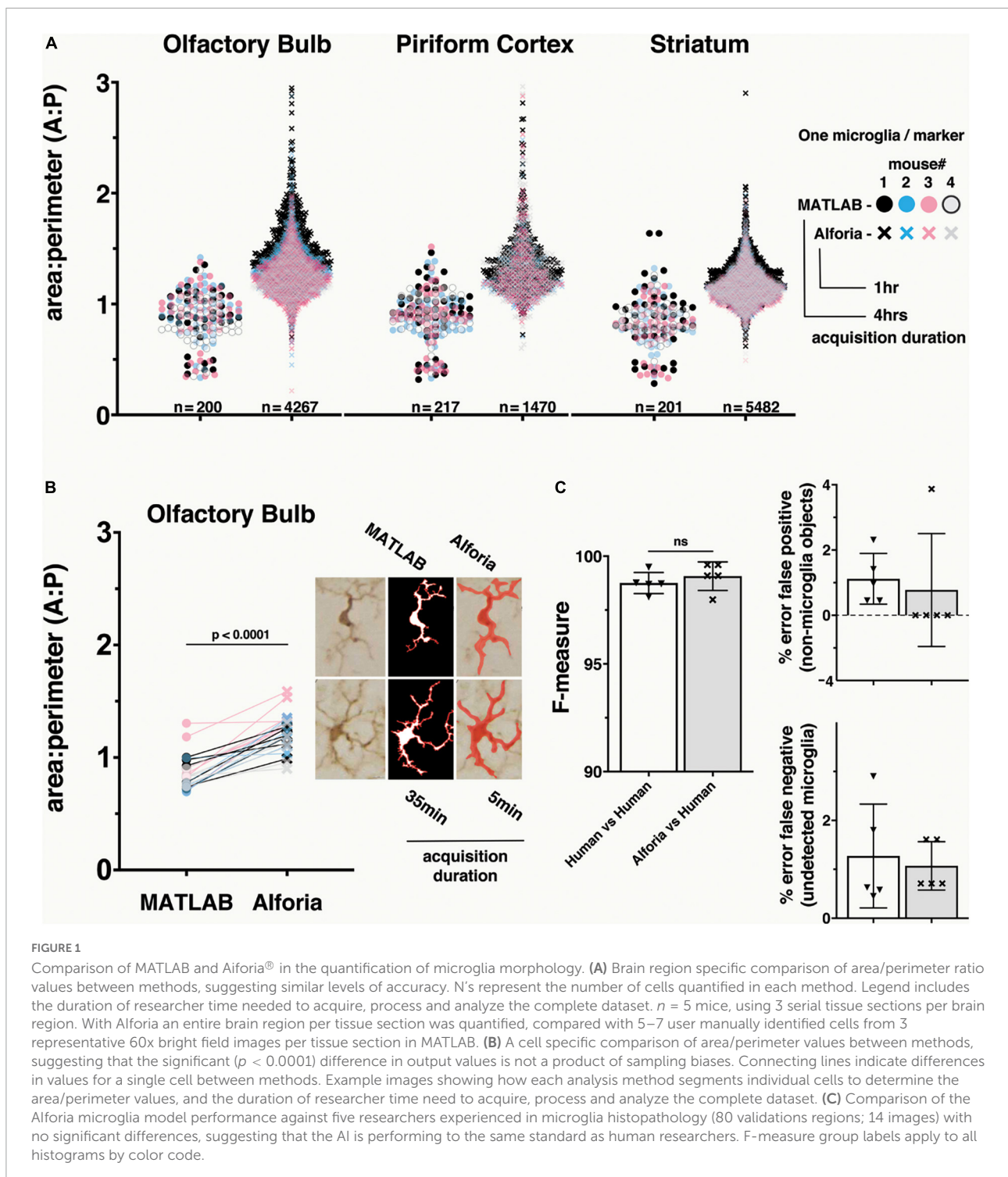
Previous studies have demonstrated the area/perimeter ratio of microglia as a reliable means for identifying microglia phenotype and the quantification of the area/perimeter ratio using semi-automated methods (George et al., 2019, 2021). Hence, the area/perimeter ratio was included for the comparison of morphology assessment methods, MATLAB and Aiforia®. First, tissue sections were selected from 4 mice from the αSyn induced olfactory dysfunction mouse model in each of the following brain regions: the inner plexiform layer of the OB, anterior piriform cortex, and dorsal striatum. For each brain region, 3 sections of tissue were selected for inclusion in the comparison dataset and were analyzed by the semi-automated MATLAB script as well as the Aiforia® Iba1-microglia detection model.

Using Aiforia®, analysis regions were defined for each serial tissue section to include the entirety of each brain region, as opposed to the three fields of view used for MATLAB (Paxinos and Franklin, 1998), and were then analyzed using the combined tissue plus Iba1-microglia AI model (**Figure 1A**). Analysis using the semi-automated MATLAB script was performed as previously described (Heindl et al., 2018). In brief, microglia were sampled from each brain region in each mouse using three fields of view per serial tissue section with a total of ∼5–8 cells per field of view.

To determine if there are differences in how each method calculates the area/perimeter ratio, a subset of 5 cells from the OB of each mouse was used for a cell-to-cell paired comparison between assessment methods. Finally, to evaluate the relative efficiency of each method, the timestamps related to dataset acquisition were reviewed and quantified in hours and minutes.

Details of model adaptation across independently collected Iba1+ datasets

To evaluate how well the microglia detection model can be adapted to additional datasets, images and layer-specific annotations were added to the original training dataset to generate additional microglia detection models. From the original αSyn induced olfactory dysfunction (i.e., "parent") model, 2 additional detection models were adapted: striatal αSyn aggregation and viral infection. To adapt the model to the new datasets, 3–5 analysis regions were annotated per image for 16 images specific to the viral infection model. Compared to the other datasets, the striatal αSyn aggregation dataset had some variability in background staining and thus 57 analysis regions were annotated across 12 images. Following annotations, a preliminary version of each model was trained using 1,500 training iterations and results were visually reviewed to estimate model performance in tissue detection, microglia detection and microglia segmentation. For the viral infection dataset, there were no errors in tissue detection, and thus no tissue layer annotations were needed. However, to ensure accurate detection of the tissue layer for the striatal αSyn aggregation model, each training image included 3.3 positive tissue signal, 3.9

FIGURE 1

Comparison of MATLAB and Aiforia® in the quantification of microglia morphology. **(A)** Brain region specific comparison of area/perimeter ratio values between methods, suggesting similar levels of accuracy. N's represent the number of cells quantified in each method. Legend includes the duration of researcher time needed to acquire, process and analyze the complete dataset. $n = 5$ mice, using 3 serial tissue sections per brain region. With Alforia an entire brain region per tissue section was quantified, compared with 5–7 user manually identified cells from 3 representative 60x bright field images per tissue section in MATLAB. **(B)** A cell specific comparison of area/perimeter values between methods, suggesting that the significant ($p < 0.0001$) difference in output values is not a product of sampling biases. Connecting lines indicate differences in values for a single cell between methods. Example images showing how each analysis method segments individual cells to determine the area/perimeter values, and the duration of researcher time need to acquire, process and analyze the complete dataset. **(C)** Comparison of the Alforia microglia model performance against five researchers experienced in microglia histopathology (80 validations regions; 14 images) with no significant differences, suggesting that the AI is performing to the same standard as human researchers. F-measure group labels apply to all histograms by color code.

background and 1 positive-signal/background interface training regions, on average.

To adapt the microglia detection layers, analysis regions were reviewed, and undetected microglia were annotated following the "small training region" strategy, annotating 2–4 microglia per region. To help eliminate the occurrence of

false positives, cell-background training regions were annotated to include additional examples of background extracellular space. On average across training images for the viral infection model, 17 cell-background and 40 small training regions were annotated along with 46 microglia, 9 of which were annotated for microglia instance segmentation. To control

for differences in background staining throughout the striatal αSyn aggregation dataset, only broad area of interest training regions were used across 7 training images. Finally, for the striatal αSyn aggregation model, 2.6 broad area of interest training regions were annotated across a range of brain regions, with 143 annotated microglia, 3 of which were annotated for microglia instance segmentation, on average across training images. Importantly, to eliminate the occurrence of false positives that result from the incorrect identification of a single microglia as two or more objects, training regions were carefully drawn/edited to exclude any overlapping portions of the object annotations (*see* **Table 1** *example training region images*).

For the final versions of each model, post-training object detection gain settings, as well as instance segmentation gain and level of detail settings, were adjusted to optimize model performance. The final version of the viral infection model completed after 60,000 training iterations using *ultra complex* instance segmentation network complexity, post-training object detection gain set to 1.4496, and instance segmentation gain set to 4 with *High* level of detail. The final version of the striatal αSyn aggregation model completed after 20,000 training iterations using *ultra complex* instance segmentation network complexity, post-training object detection gain set to 1.25, instance segmentation gain set to 3.75 with *High* level of detail (**Supplementary Figure 1B**).

Validating adapted models across independent Iba1+ datasets using Aiforia®

To validate the accuracy of our "parent" microglia detection model (αSyn induced olfactory dysfunction) we compared microglia detection by the AI model with manual annotations of microglia in 80 validation areas across images containing 4-10 microglia from 14 animals excluded from the training data. Validation annotations were manually entered by 4–5 researchers experienced in identifying microglia across a range of functional states. These annotations were then compared to the model's analysis results (AIforia vs. human), as well as the annotations of each individual researcher (human vs. human), to determine if the model's performance matched that of human researchers. The features quantified for this comparison include non-microglia detected as microglia (false positive), undetected microglia (false negative), space-dependent overlap of analysis results with human annotations (precision), space-independent overlap of analysis results with annotations (sensitivity), and F-measure (the harmonic mean of precision and sensitivity) (Penttinen et al., 2018; Mäkelä et al., 2021). The AI model was considered valid when the AI vs human results performed equal to or better than human vs human (interobservability) results on average. Next, to demonstrate the limitations of generalizability and the importance of training data in adapting the microglia detection model, each adapted model was validated against manual annotations from researchers, as in the method described above. For validating across independent

Iba1+ datasets, the number of validation regions was increased to 330 across 25 images equally representing each of the datasets, as well as 2 additional datasets that were not part of the training data for any of the models.

Handling of generated data

Data outputs from Aiforia® were post-processed in Rstudio (ver.1.4.1106) primarily to calculate the area/perimeter ratios as well as the mean object diameter for each analysis region. However, due to background staining variability in the striatal αSyn aggregation dataset, regions with fewer than 100 cells were filtered from the analysis (a total of 4 ROIs removed). Additionally, post-processing was performed to calculate the means of all morphology measures within a single animal for each brain region. Finally, Rstudio Notebook/markdown versions of these scripts are also available to help streamline processing of future analyses (see supporting documents).

Statistical analysis

Statistical analysis was performed using GraphPad Prism 9. Cell-to-cell results were analyzed using a Wilcoxon matched-pair signed rank test. Validation results were analyzed using an unpaired *t*-test. For the cell data from the striatal αSyn aggregation model the data ($n = 120,801$ PBS; $n = 130,906$ PFF) was standardized using default settings in GraphPad Prism 9, and analyzed using a principal component analysis 1,000 seeds and 10 variables. The type of analysis with *post hoc* correction for multiple testing is indicated in the legend of each figure.

Results

Comparison of microglia morphology assessment methods across brain regions

To evaluate how well our new microglia detection model quantifies change in microglia reactivity we compared area/perimeter ratios between our model and a custom semi-automated object-segmentation MATLAB script that had been previously published (George et al., 2019, 2021). Using histological slides from the αSyn induced olfactory dysfunction model, we analyzed 3 brain regions across 4 mice and compared the values of all cells. These results suggest that the compared methods perform similarly on identical datasets, but that the greater number of cells quantified using the Aiforia® microglia detection model may provide a more complete description of microglia reactivity in each brain region (**Figure 1A**). It is also important to note that the dataset acquisition and quantification duration for the MATLAB script was four times longer than

the AI model, which could be an important consideration when analyzing large datasets.

While the range of area/perimeter values between compared methods does not differ greatly, even a brief visual inspection of the data suggests a clear increase in area/perimeter values using the microglia detection model (**Figure 1A**). A known limitation of the semi-automated MATLAB script, and other fully automated commercially available cell morphology quantification methods, is a failure to quantify overlapping microglia as separate cells. This limitation results in a bias toward the quantification of only microglia that do not overlap, which is of special importance when studying microglia under conditions that can trigger microgliosis or increase in cell numbers and density (Schwabenland et al., 2021). To determine if this limitation could explain the difference in area/perimeter quantification between methods, we selected a subset of cells from the olfactory bulb for a paired cell-to-cell comparison between methods. The paired cell comparison results suggest that the microglia detection model values are higher as a function of the analysis and not a result of selection bias in the MATLAB script (**Figure 1B**). This is not surprising, as the branching function included to detect microglia processes in the MATLAB script can result in a bias toward higher perimeter values, resulting in lower area/perimeter values (**Supplementary Figure 2**), while the probabilistic object segmentation of microglia in the AI model can bias toward lower perimeter values (higher area/perimeter values).

Taken together these results suggest that both models are effective in quantifying the morphological parameters of individual microglia cells, and that the area/perimeter ratio for the microglia included in the comparison dataset are likely within the overlapping results of these methods. Additionally, the volume of data acquired using the AI model and the duration of time needed for data collection (**Supplementary Table 1**) make it a superior method for analyzing microglia morphology within a given brain region, especially for larger datasets common in translational and pre-clinical studies.

Validation of microglia morphology using Aiforia®

To determine if the microglia detection model performed as well as human annotators, validation regions were annotated by researchers experienced in microglia histopathology. The harmonic mean of the precision and sensitivity scores (F1 or F-measure) were used to compare each method. The F-measure values for the microglia detection model were not significantly different from the F-measure values for the human annotators (p = 0.02 Mann–Whitney U) (**Figure 1C**). It is important to note that there is some error in both human annotations (false positive: 1.1%, false negative: 1.3%) and the microglia detection mode (false positive: 0.77%, false negative: 1.1%), but while there

is a relatively even split in the error of human annotations between false positive and negative, the microglia detection model's error is mostly due to false negatives, making it the more conservative method. Taken together, these results validate the use of this new microglia detection model as a method for quantifying the number of microglia present in each region, and those results generated using this method are more conservative than human annotations.

Validation of model adaptation across Iba1+ datasets

To evaluate how well the microglia detection model can be adapted to additional datasets, images and layer-specific annotations were added to the original training dataset to generate study specific models for the quantification of Iba1+ histopathological slides from the mouse model of striatal αSyn aggregation and the mouse model of viral infection. In addition to the original αSyn induced olfactory dysfunction (i.e., "parent") model, models for striatal αSyn aggregation and viral infection were developed. To demonstrate the limitations of generalizability and the importance of training data in adapting the microglia detection model, each of the 3 models was then validated across all datasets as well as 2 additional datasets of Iba1 + histopathological slides that were not part of the training datasets for any of the 3 models: adaptive transfer, and αSyn monomer. Our results suggest that there is no significant difference between microglia detection models and human performance when the adapted model includes layer-specific annotations from the new dataset (**Figures 2A,B**; absolute mean difference in F-measure αSyn induced olfactory dysfunction 0.32 p = 0.413, striatal αSyn aggregation 1.40 p = 0.588, viral infection 0.25 p = 0.66). As predicted, models generally performed better on datasets that were included in the layer specific example training data for that model. However, the striatal αSyn aggregation model performed better on the αSyn induced olfactory dysfunction dataset, which is not surprising as this model was adapted from the αSyn induced olfactory dysfunction model and includes more training examples that span a wider range of background staining variability (**Figure 2B**; absolute mean difference in F-measure 0.09 p = 0.899). Interestingly, the αSyn induced olfactory dysfunction model was able to generalize to the adaptive transfer dataset, which did not contribute to the example training data for that model (**Figure 2B**; absolute mean difference in F-measure 0.19 p = 0.888). Overall, these results reinforce the importance of incorporating layer-specific training examples when adapting the microglia detection model to a new study. Additionally, the performance of the αSyn induced olfactory dysfunction model on the adaptive transfer dataset suggests that in some instances a model can be robust enough to accurately quantify datasets in the absence of additional training
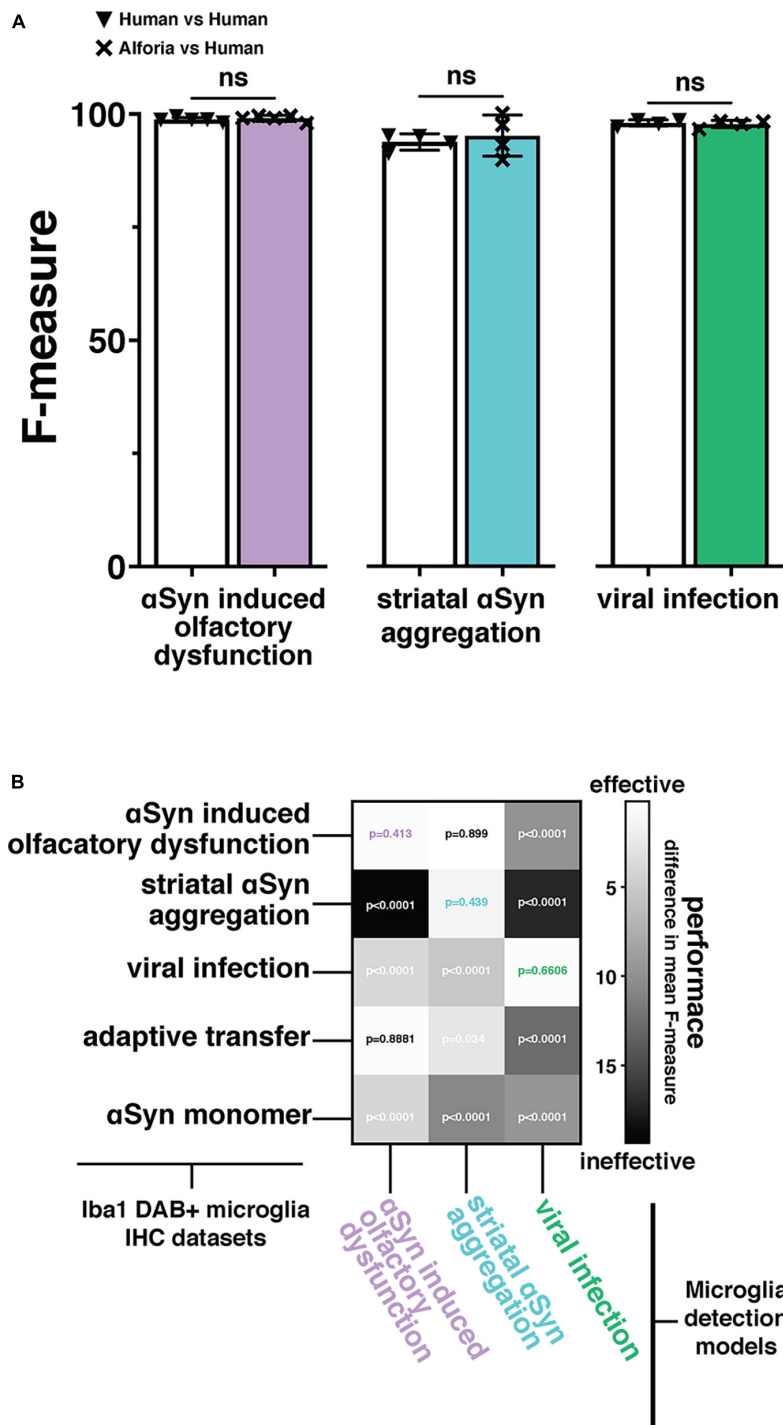
FIGURE 2
Adaptation and validation of the microglia model across independently collected datasets. **(A)** Comparison of the original (αSyn induced olfactory dysfunction) and adapted (striatal αSyn aggregation and viral infection) Aiforia® microglia models' performances (F-measure) against researchers experienced in microglia histopathology with no significant differences, suggesting that the AI is performing to the same standard as human researchers (αSyn induced olfactory dysfunction: 80 validations regions across 14 images, striatal αSyn aggregation 42 validations regions, 25 images, and viral infection: 50 validation regions across 5 images). **(B)** Two-dimensional histogram using the difference in mean F-measure between each model's output performance and 4−5 researchers experienced in microglia histopathology across five independently collected datasets, to emphasize the importance of adapting the microglia model to a new dataset. *P*-values associated with the difference in F-measure between AI models and human annotations included at the intersections of Iba1 + microglia immunohistochemistry (IHC) staining datasets, and microglia detection models. *P*-values using color coded specific highlights indicate the performance of a dataset specific model adaptation and are represented as "ns" in "A".

data, as the adaptive transfer dataset was not a part of the training data for any of the models.

Quantifying viral infection induced change in microglia reactivity

To determine if validating the microglia detection models to a similar standard would allow for the comparison of fully independent datasets, we compared the results of the viral infection dataset with PBS sham injected animals in the αSyn induced olfactory dysfunction dataset. Viral infections are known to cause inflammation and change in microglia reactivity in the CNS (Zhou et al., 2008; Erny et al., 2015; Rua et al., 2019), while the intracranial injections of PBS in the olfactory bulb do not (Rey et al., 2016; Johnson et al., 2020). As predicted, the analysis results in each of these datasets fall within a similar range across all measures, with a clear separation of values between the two datasets that suggests a change in microglia reactivity as a result of viral infection but not from the PBS sham injections (**Figure 3A**). When normalizing counts of Iba1+ microglia to striatum tissue area, there is a clear increase in counts in virus infected mice compared to the PBS sham mice (**Figure 3A**). Additionally, when comparing the area/perimeter values and the cell diameters, the results of the viral infection analysis suggest higher area/perimeter values and lower cell diameters when compared to the PBS sham group (**Figure 3B**). Finally, when comparing area/perimeter, cell diameters and counts separated by treatment groups, these data clearly fall into a similar range of values and remain consistent with the prediction that the viral infection will result in more change in microglia reactivity when compared to the PBS sham injection (**Figure 3B**, inset histograms). These results suggest that it is possible to compare independently collected datasets by adapting the microglia detection model to each dataset and validating these models to a similar standard.

Quantifying microglia morphology in a mouse model of striatal αSyn injection

To determine if the microglia detection model can be effectively adapted to quantify microglial functional state across labs, histopathological slides from a different mouse model of αSyn aggregation were used. This model, based on the intrastriatal injection of αSyn PFFs, is characterized by changes in microglia morphology with minimal effects on the total number of cells, a finding that is consistent with mouse models using intrastriatal injections of AAVs to produce αSyn aggregation (George et al., 2019, 2021).

First, the "parental" microglia model was adapted to the new images and validated against human annotators experienced in identifying microglia. The validation results for the striatal αSyn
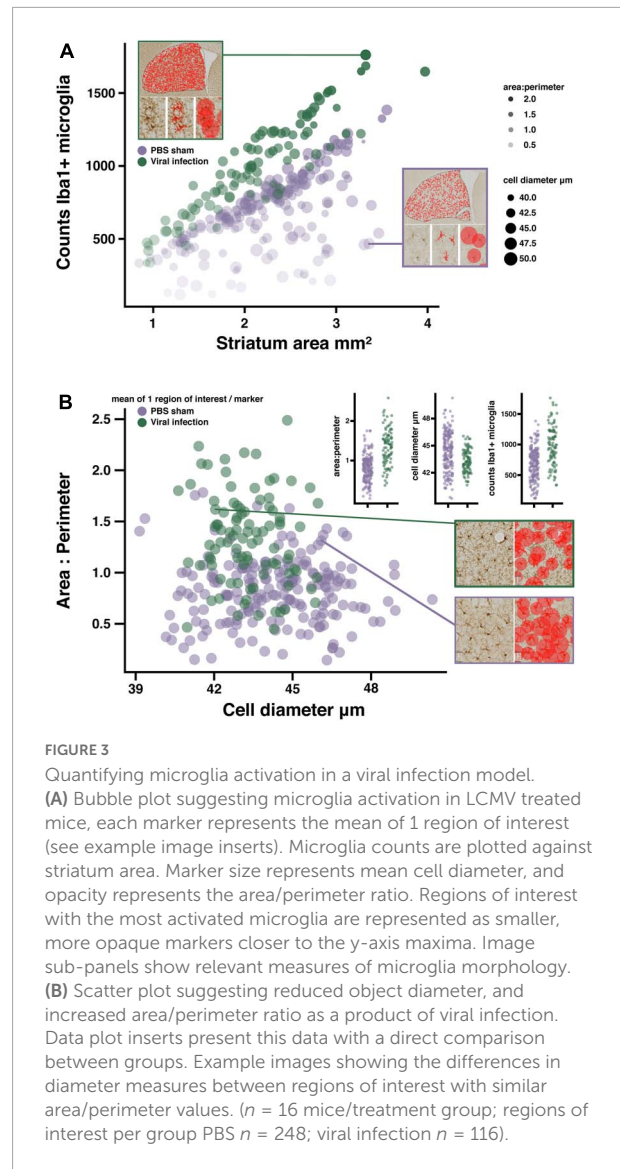

FIGURE 3

Quantifying microglia activation in a viral infection model. **(A)** Bubble plot suggesting microglia activation in LCMV treated mice, each marker represents the mean of 1 region of interest (see example image inserts). Microglia counts are plotted against striatum area. Marker size represents mean cell diameter, and opacity represents the area/perimeter ratio. Regions of interest with the most activated microglia are represented as smaller, more opaque markers closer to the y-axis maxima. Image sub-panels show relevant measures of microglia morphology. **(B)** Scatter plot suggesting reduced object diameter, and increased area/perimeter ratio as a product of viral infection. Data plot inserts present this data with a direct comparison between groups. Example images showing the differences in diameter measures between regions of interest with similar area/perimeter values. ($n = 16$ mice/treatment group; regions of interest per group PBS $n = 248$; viral infection $n = 116$).

aggregation model suggest that there is no significant difference between AI performance and human annotations (**Figure 4A**). Next, 6 brain regions were analyzed, including: striatum, motor cortex, hippocampus, cingulate cortex, paraventricular nucleus of the hypothalamus (PVN), and the piriform cortex. Some of these regions are known to be affected in this mouse model, specifically the striatum and the motor cortex (Earls et al., 2019; Dutta et al., 2021). From this analysis, the mean cell values from each region of interest were plotted irrespective of brain region to visualize any differences between PBS and PFF groups as a whole. As predicted, these results suggest that there are increases in the area/perimeter ratio in the microglia of animals injected with PFFs as compared to animals injected with PBS, and that there is no clear difference in the number of microglia (**Figure 4B**). To determine if there are region specific effects of treatment, a more conventional presentation of the data was
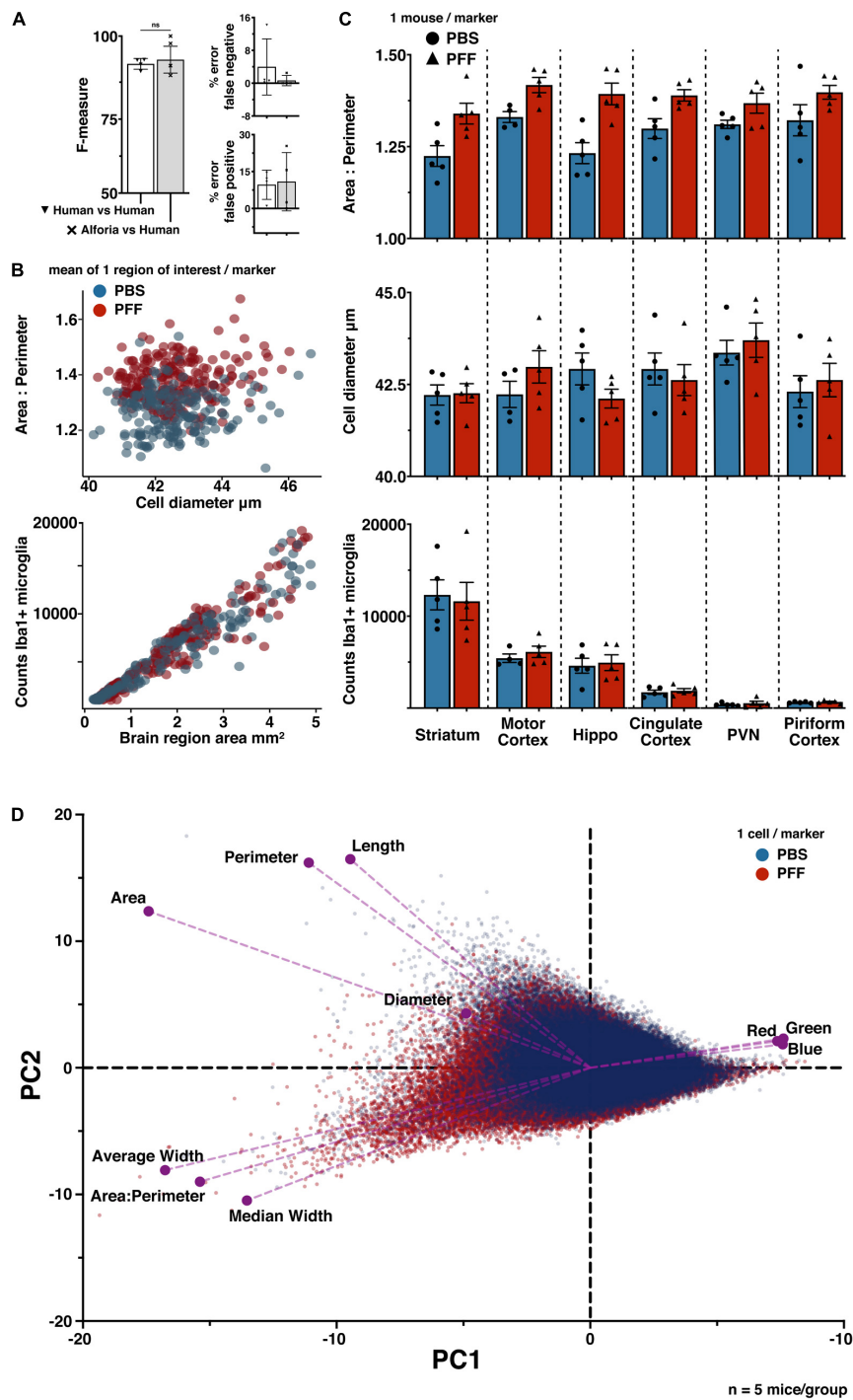
FIGURE 4

Quantifying microglia activation in a model of striatal αSyn aggregation. **(A)** Comparison of striatal αSyn aggregation microglia adapted model performance against researchers experienced in microglia histopathology (42 validations regions, 25 images), with no significant differences. **(B)** PFFs are related to changes in microglia morphology (scatter plot 1), but not the number of cells (scatter plot 2). The number of regions of interest were selected to sample evenly across mice within each brain region. Each marker represents 1 region of interest: cingulate cortex (*n* = 82), hippocampus (*n* = 77), motor cortex (*n* = 75), paraventricular nucleus (PVN) (*n* = 30), piriform cortex (*n* = 35), striatum (n = 120). (*n* = 5 mice/treatment group; regions of interest per group PBS *n* = 204; PFF *n* = 220). **(C)** Comparison of microglia morphology measures across brain regions, suggesting an effect of treatment on microglia morphology but no effect on the number of microglia. Each marker represents one animal, error bars represent within group standard mean errors (*n* = 5 mice/treatment group). **(D)** Principal component analysis biplot confirming a treatment specific data separation, with respect to each measure of microglia morphology; area:perimeter, area, perimeter, diameter, color channel values (Red, Green, Blue), length, average width, and median width (PBS n = 120,801; PFF n = 130,906).

utilized, reducing the data to a single value for each animal in each brain region (**Figure 4C**). The brain region specific results are consistent again with previous findings that intrastriatal injections of PFFs are linked to an increase in area/perimeter ratio of microglia but not cell diameter or the total number of microglia, across all regions (George et al., 2019, 2021).

Finally, to further explore how the measured dimensions of morphology contribute to variability across treatment groups, a principle component analysis was performed using the raw cell-data ($n = 120,801$ PBS; $n = 130,906$ PFF) (**Figure 4D**). These results confirm that the area/perimeter ratio and the cell diameter are defining features of microglia functional state. They also suggest that the cell length and width measurements, quantified by default in the Aiforia® platform, may provide similarly effective characterization of microglia phenotype.
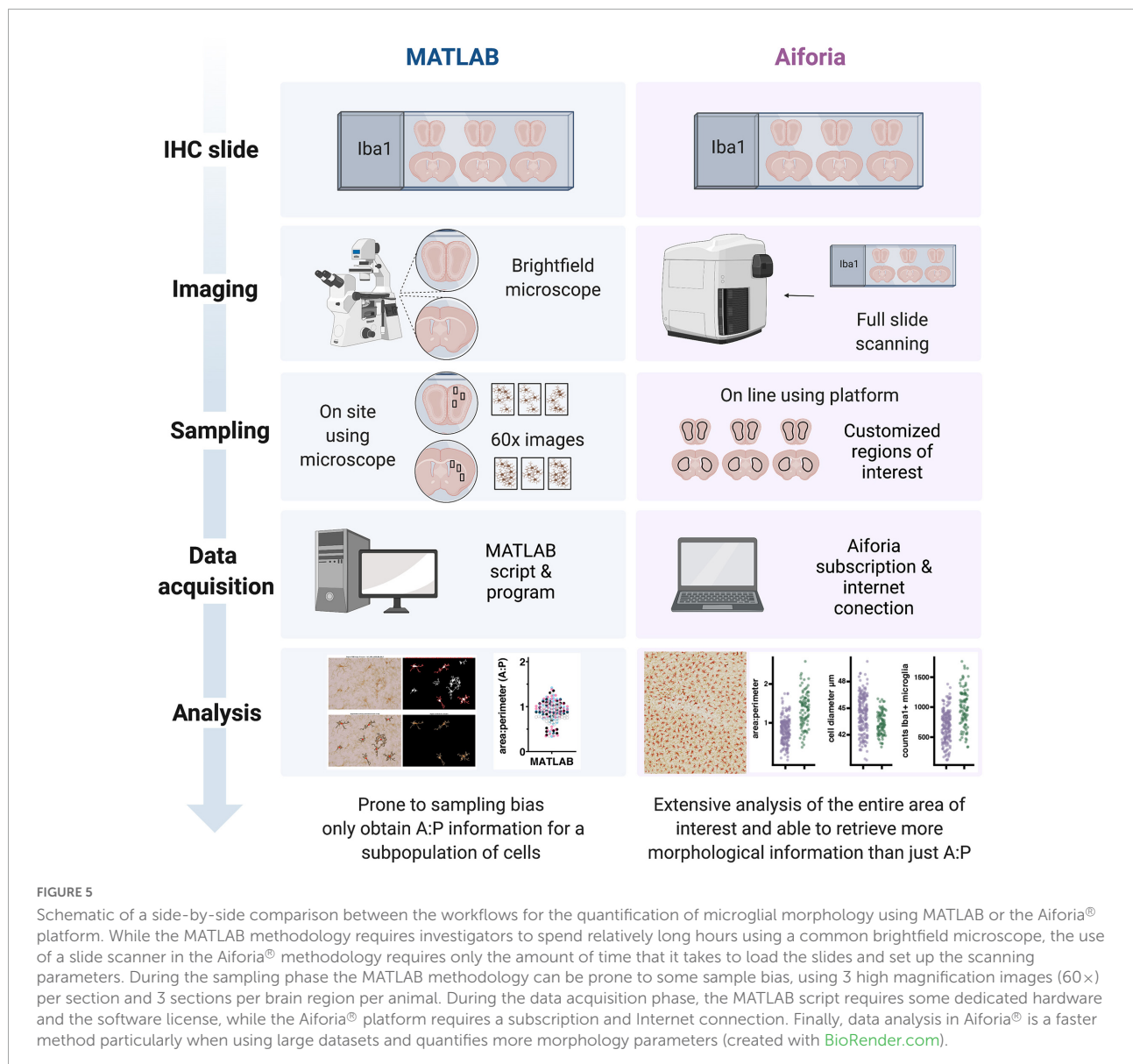
Discussion

Here we describe the use of commercially available deep learning tools to quantify microglia counts and morphology from histopathological tissue sections stained for Iba1. We provide the application of this method across a range of independently collected datasets and compare results from our previously published method with this new machine learning approach. Using an automated multi-measure approach to rapidly quantify nearly all change in microglia reactivity for a given region using only a single immunohistochemistry staining label can be appealing for a variety of reasons (**Figure 5**). The sampling capacity can enable a more complete and reliable description of treatment effects, and the number of morphological measures quantified increases the dimensionality of data, permitting researchers to explore new questions while streamlining existing projects. However, there are additional considerations that are essential for the efficiency of any study. Limitations intrinsic to methods that are dependent on dedicated workstations include: user access, obsolescing dependencies, specialized hardware, and in some instances extensive training. These limitations can be a strong incentive to apply flexible, cloud-based, user-friendly platforms (Kagadis et al., 2013; Herculano-Houzel et al., 2015). These platforms also provide the most efficient means of transparent reproducible analyses as well as options for collaboration. The work presented here details a platform-dependent workflow for quantifying microglia morphology that performs to the standard of human observation and can be applied across independently collected datasets.

The cloud-based platform Aiforia® enabled us to develop a robust microglia detection model that we could generalize across 2 additional datasets, each with its own model. Dataset specific generalization optimizes model performance in each of the adapted datasets (**Figure 2B**). We then validated these models at or above human performance. Validating a model

to a specific standard can allow for the direct comparison of results from independent sources (Plis et al., 2014; Liu et al., 2019). Using human observations as the standard could make results more reproducible by reducing variability related to analysis specific parameters that may not generalize across independently collected datasets. Finally, using these models we found that it was possible to quantify changes in microglia morphology that are consistent with previous observations in mouse models of viral infection (Erny et al., 2015), and αSyn aggregation (Kagadis et al., 2013; Herculano-Houzel et al., 2015). Furthermore, the increased sampling capacity of these microglia models relative to previously published methods (George et al., 2019) expanded the quantification of Iba1+ microglia to a scale more commonly applied in other areas of bioinformatics such as proteomics (Boekweg et al., 2021). While there are other automated methods of microglia morphology quantification (York et al., 2018; Clarke et al., 2021; Gober et al., 2022) and potentially more sophisticated study-specific AI models (Kyriazis et al., 2019; Bascuñana et al., 2020; Leyh et al., 2021; Möhle et al., 2021), the methods we now describe offer a streamlined workflow for meaningful results and an accessibility to flexible deep learning tools that could be appealing to researchers without formal computer science training.

One challenge of developing this model using commercially available tools is that there is no option for user customization of the platform. Where many study-specific AI models include elements of conventional programming to derive features related to the number of processes and their branching index (Garcia-Segura and Perez-Marquez, 2014; Fernández-Arjona et al., 2017), those options are not currently user accessible in Aiforia®. That said, it is possible that these features are intentionally excluded to streamline the platform as the tools included in Aiforia® should be sufficient to quantify these morphological features. However, doing so is currently outside the scope of this study. Additionally, while microglia identification, quantification of total microglia and microglia morphology were fully automated, the analysis regions were manually annotated. Currently there is no measure of control for the variability introduced by the inconsistencies inherent to manual sampling of specific brain regions, but it is likely that this will also be automated in future models.

Finally, the models developed for this study did not establish categories of different ramification microglia types (Garcia-Segura and Perez-Marquez, 2014). While these classifications can be helpful, the goal of this microglia model was to create a reliable quantification of the microglia area/perimeter ratio that could be easily applied across independent datasets. It is important to note that a model using 6 categories of different ramification types was validated prior to the models presented here, and the 6-category model is also available in the Aiforia® platform. While the models discussed here effectively quantify Iba1+ microglia they are unlikely to quantify microglia morphology using immunofluorescent markers or

FIGURE 5
Schematic of a side-by-side comparison between the workflows for the quantification of microglial morphology using MATLAB or the Aiforia®
platform. While the MATLAB methodology requires investigators to spend relatively long hours using a common brightfield microscope, the use
of a slide scanner in the Aiforia® methodology requires only the amount of time that it takes to load the slides and set up the scanning
parameters. During the sampling phase the MATLAB methodology can be prone to some sample bias, using 3 high magnification images (60×)
per section and 3 sections per brain region per animal. During the data acquisition phase, the MATLAB script requires some dedicated hardware
and the software license, while the Aiforia® platform requires a subscription and Internet connection. Finally, data analysis in Aiforia® is a faster
method particularly when using large datasets and quantifies more morphology parameters (created with BioRender.com).

immunohistochemical makers other than Iba1 (e.g., P2RY12, CX3CR1, CD11b). However, using the methods described here it would be possible for a researcher to develop their own microglia models with any combination of techniques commonly used to image microglia, as well as the use of additional stains to include astrocytes or neurons. Creating a new model only requires an Aiforia® subscription, internet connection, and high-quality images.

Conclusion

Using commercially available deep learning tools, we developed a method for quantifying Iba1+ microglia morphology, which we validated at or above human performance, and adapted to analyze microglia functional state in mouse models for viral infections and αSyn aggregation. By all quantified measures of microglia morphology, the analysis results presented here are consistent with those previously published. Furthermore, by validating each deep learning model to the same standard we were able to potentially reduce the variability intrinsic to independently collected datasets. In addition, timestamped activity logs suggest the dataset acquisition duration is conservatively four times faster than our previously published MATLAB method, and the total number of microglia quantified shows a percent increase of 577–2627%. While the deep learning tools used for the method discussed here are commercially available on a cloud-based platform, developing generalizable deep learning models can be labor intensive. Here, we provide 4 robust models for

quantifying microglia morphology that are available in the Aiforia® platform, for study-specific adaptation.

Data availability statement

The datasets presented in this study can be found in online repositories. The name of the repository and accession number can be found below: GitHub, https://github.com/LucasStetzik/Supportingdata_AIforia_Iba1.

Ethics statement

The animal study was reviewed and approved by Van Andel Institute's Institutional Animal Care and Use Committee.

Author contributions

LSt and GM wrote the manuscript. LSt performed morphological data collection, deep learning assisted model development, and data analysis. LSt, GM, LSm, EQ, and SG validated the models. PB supervised this study, provided expertise and advice, and provided tissue for the αSyn induced olfactory dysfunction model and the PBS sham tissue used as the control in the Viral infection model, as well as tissue for the adaptive transfer dataset and the αSyn monomer dataset. GM, ES, LM, AL, and KL performed animal treatment and testing, collected tissue, and performed brain sectioning. GM performed brain sectioning and IHC. SG, ES, LM, AL, and AB performed animal treatment and testing, collected tissue, performed brain sectioning, and IHC. RJ provided the tissue for the LCMV infected mice in the viral infection model. JP provided the tissue for the striatal αSyn aggregation model. LSt, GM, and EQ imaged all tissue slides. MH, RJ, LB, JP, and PB provided necessary support and feedback. All authors reviewed and edited the manuscript.

Conflict of interest

PB receives commercial support as a consultant from Axial Therapeutics, Calico Life Sciences, CureSen, Enterin Inc, Idorsia Pharmaceuticals, Lundbeck A/S, AbbVie, Fujifilm-Cellular Dynamics International. He has received commercial support for research from Lundbeck A/S and Roche. He has ownership interests in Acousort AB, Enterin Inc and RYNE Biotechnology. RJ is an advisor for Agios Pharmaceuticals and Servier Pharmaceuticals. He is a member of the scientific advisory board and has ownership interests in Immunomet Therapeutics. Author LSm was employed by Aiforia Technologies.

The remaining authors declare that the research was conducted in the absence of any commercial or financial relationships that could be construed as a potential conflict of interest.

Publisher's note

All claims expressed in this article are solely those of the authors and do not necessarily represent those of their affiliated organizations, or those of the publisher, the editors and the reviewers. Any product that may be evaluated in this article, or claim that may be made by its manufacturer, is not guaranteed or endorsed by the publisher.

Supplementary material

The Supplementary Material for this article can be found online at: https://www.frontiersin.org/articles/10.3389/fncel.2022.944875/full#supplementary-material

SUPPLEMENTARY FIGURE 1
Workflows for the development and adaptation of deep learning assisted models for microglial morphology assessment using Aiforia®. **(A)** Workflow for the development of microglial morphology assessment model. The "parental" model was developed with a subset of 35 IHC anti-Iba1 slides from a mouse model of αSyn induced olfactory dysfunction used for training input data (see **Table 1**). Details for the final round of iterations and the CNN settings by feature layer are included (network complexity, field of view, post training gains, etc.). After training, a new subset of slides (not used during the training phase) was used for validation, and cell examples were used to compare the model performance against 4–5 researchers experienced in microglial histology. **(B)** Workflow for the adaptation of the "parental" model to

independently acquired datasets. Project-specific AIs were adapted by including additional IHC training data from mouse models of (1) viral infection and (2) striatal αSyn aggregation, to the "parental" model training data. Pre-training parameters were the same as in the "parental" model, and post-training parameters were optimized for object detection and instance segmentation as shown for each of the adapted models. New slides (not included in the training data) were used during validation against researchers experienced in microglial histology. Validated models were released and used for the quantification of microglial morphology from the Iba1 stain slides from all three mouse models. By validating each model to the same standard, analysis results were comparable (created with BioRender.com).

SUPPLEMENTARY FIGURE 2
Comparison of area and perimeter values between MATLAB and Aiforia®. Olfactory bulb Iba1 + microglia area/perimeter ratio, area, and perimeter values across 4 mice between methods, suggesting differences in area/perimeter ratio values are possibly the result of differences in perimeter value quantifications. Each histogram includes data from 1 mouse, each marker represents the values for one cell. Data collected using MATLAB represented in white bars, data collected using Aiforia® in gray.

References

Awogbindin, I. O., Ishola, I. O., St-Pierre, M. K., Carrier, M., Savage, J. C., Paolo, T. D., et al. (2020). Remodeling microglia to a protective phenotype in Parkinson's disease? *Neurosci. Lett.* 735:135164.

Bascuñana, P., Brackhan, M., and Pahnke, J. (2020). Machine learning-supported analyses improve quantitative histological assessments of amyloid-β deposits and activated microglia. *J. Alzheimers Dis.* 79, 597–605. doi: 10.3233/JAD-201120

Battegay, M., Cooper, S., Althage, A., Bänziger, J., Hengartner, H., and Zinkernagel, R. M. (1991). Quantification of lymphocytic choriomeningitis virus with an immunological focus assay in 24- or 96-well plates. *J. Virol. Methods* 33, 191–198.

Boekweg, H., Guise, A. J., Plowey, E. D., Kelly, R. T., and Payne, S. H. (2021). Calculating sample size requirements for temporal dynamics in single-cell proteomics. *Mol. Cell. Proteom.* 20:100085. doi: 10.1016/j.mcpro.2021.100085

Clarke, D., Crombag, H. S., and Hall, C. N. (2021). An open-source pipeline for analysing changes in microglial morphology. *Open Biol.* 11:210045. doi: 10.1098/rsob.210045

Colton, C. A., and Wilcock, D. M. (2010). Assessing activation states in microglia. *CNS Neurol. Disord. Drug Targets* 9, 174–191.

Davis, E. J., Foster, T. D., and Thomas, W. E. (1994). Cellular forms and functions of brain microglia. *Brain Res. Bull.* 34, 73–78.

Dutta, D., Jana, M., Majumder, M., Mondal, S., Roy, A., and Pahan, K. (2021). Selective targeting of the TLR2/MyD88/NF-κB pathway reduces α-synuclein spreading in vitro and in vivo. *Nat. Commun.* 12:5382.

Earls, R. H., Menees, K. B., Chung, J., Barber, J., Gutekunst, C. A., Hazim, M. G., et al. (2019). Intrastriatal injection of preformed alpha-synuclein fibrils alters central and peripheral immune cell profiles in non-transgenic mice. *J. Neuroinflamm.* 16:250. doi: 10.1186/s12974-019-1636-8

Erny, D., de Angelis, A. L. H., Jaitin, D., Wieghofer, P., Staszewski, O., David, E., et al. (2015). Host microbiota constantly control maturation and function of microglia in the CNS. *Nat. Neurosci.* 18, 965–977. doi: 10.1038/nn.4030

Fernández-Arjona, M. D. M., Grondona, J. M., Granados-Durán, P., Fernández-Llebrez, P., and López-Ávalos, M. D. (2017). Microglia morphological categorization in a rat model of neuroinflammation by hierarchical cluster and principal components analysis. *Front. Cell. Neurosci.* 11:235. doi: 10.3389/fncel.2017.00235

Ferreira, T. A., Blackman, A. V., Oyrer, J., Jayabal, S., Chung, A. J., Watt, A. J., et al. (2014). Neuronal morphometry directly from bitmap images. *Nat. Methods* 11, 982–984. doi: 10.1038/nmeth.3125

Garcia-Segura, L. M., and Perez-Marquez, J. (2014). A new mathematical function to evaluate neuronal morphology using the Sholl analysis. *J. Neurosci. Methods* 226, 103–109. doi: 10.1016/j.jneumeth.2014.01.016

George, S., Rey, N. L., Tyson, T., Esquibel, C., Meyerdirk, L., Schulz, E., et al. (2019). Microglia affect α-synuclein cell-to-cell transfer in a mouse model of Parkinson's disease. *Mol. Neurodegener.* 14:34. doi: 10.1186/s13024-019-0335-3

George, S., Tyson, T., Rey, N. L., Sheridan, R., Peelaerts, W., Becker, K., et al. (2021). T cells limit accumulation of aggregate pathology following intrastriatal injection of α-synuclein fibrils. *J. Parkinsons Dis.* 11, 585–603. doi: 10.3233/JPD-202351

Gober, R., Ardalan, M., Shiadeh, S. M. J., Duque, L., Garamszegi, S. P., Ascona, M., et al. (2022). Microglia activation in postmortem brains with schizophrenia demonstrates distinct morphological changes between brain regions. *Brain Pathol.* 32:e13003. doi: 10.1111/bpa.13003

Heindl, S., Gesierich, B., Benakis, C., Llovera, G., Duering, M., and Liesz, A. (2018). Automated morphological analysis of microglia after stroke. *Front. Cell. Neurosci.* 12:106. doi: 10.3389/fncel.2018.00106

Herculano-Houzel, S., von Bartheld, C. S., Miller, D. J., and Kaas, J. H. (2015). How to count cells: The advantages and disadvantages of the isotropic fractionator compared with stereology. *Cell Tissue Res.* 360, 29–42. doi: 10.1007/s00441-015-2127-6

Ito, D., Imai, Y., Ohsawa, K., Nakajima, K., Fukuuchi, Y., and Kohsaka, S. (1998). Microglia-specific localisation of a novel calcium binding protein, Iba1. *Mol. Brain Res.* 57, 1–9. doi: 10.1016/s0169-328x(98)00040-0

Johnson, M. E., Bergkvist, L., Mercado, G., Stetzik, L., Meyerdirk, L., Wolfrum, E., et al. (2020). Deficits in olfactory sensitivity in a mouse model of Parkinson's disease revealed by plethysmography of odor-evoked sniffing. *Sci. Rep.* 10:9242. doi: 10.1038/s41598-020-66201-8

Johnson, M. E., Bergkvist, L., Stetzik, L., Steiner, J. A., Meyerdirk, L., Schulz, E., et al. (2021). Heterozygous GBA D409V and ATP13a2 mutations do not exacerbate pathological α-synuclein spread in the prodromal preformed fibrils model in young mice. *Neurobiol. Dis.* 159:105513. doi: 10.1016/j.nbd.2021.105513

Kagadis, G. C., Kloukinas, C., Moore, K., Philbin, J., Papadimitroulas, P., Alexakos, C., et al. (2013). Cloud computing in medical imaging. *Med. Phys.* 40:070901.

Kolosowska, N., Gotkiewicz, M., Dhungana, H., Giudice, L., Giugno, R., Box, D., et al. (2020). Intracerebral overexpression of miR-669c is protective in mouse ischemic stroke model by targeting MyD88 and inducing alternative microglial/macrophage activation. *J. Neuroinflamm.* 17:194. doi: 10.1186/s12974-020-01870-w

Kongsui, R., Johnson, S. J., Graham, B. A., Nilsson, M., and Walker, F. R. (2015). A combined cumulative threshold spectra and digital reconstruction analysis reveal structural alterations of microglia within the prefrontal cortex following low-dose LPS administration. *Neuroscience* 310, 629–640.

Kyriazis, A. D., Noroozizadeh, S., Refaee, A., Choi, W., Chu, L. T., Bashir, A., et al. (2019). An end-to-end system for automatic characterization of iba1

immunopositive microglia in whole slide imaging. *Neuroinformatics* 17, 373–389. doi: 10.1007/s12021-018-9405-x

Leyh, J., Paeschke, S., Mages, B., Michalski, D., Nowicki, M., Bechmann, I., et al. (2021). Classification of microglial morphological phenotypes using machine learning. *Front. Cell. Neurosci.* 15:701673. doi: 10.3389/fncel.2021.701673

Lier, J., Streit, W. J., and Bechmann, I. (2021). Beyond activation: Characterizing microglial functional phenotypes. *Cells* 10:2236.

Liu, X., Faes, L., Kale, A. U., Wagner, S. K., Fu, D. J., Bruynseels, A., et al. (2019). A comparison of deep learning performance against health-care professionals in detecting diseases from medical imaging: A systematic review and meta-analysis. *Lancet Digit. Health* 1, e271–e297. doi: 10.1016/S2589-7500(19)30123-2

Mäkelä, K., Mäyränpää, M. I., Sihvo, H. K., Bergman, P., Sutinen, E., Ollila, H., et al. (2021). Artificial intelligence identifies inflammation and confirms fibroblast foci as prognostic tissue biomarkers in idiopathic pulmonary fibrosis. *Hum. Pathol.* 107, 58–68. doi: 10.1016/j.humpath.2020.10.008

Möhle, L., Bascuñana, P., Brackhan, M., and Pahnke, J. (2021). Development of deep learning models for microglia analyses in brain tissue using DeePathology™ STUDIO. *J. Neurosci. Methods* 364:109371.

Nakajima, K., and Kohsaka, S. (2001). Microglia: Activation and their significance in the central nervous system. *J. Biochem.* 130, 169–175.

Ohsawa, K., Imai, Y., Kanazawa, H., Sasaki, Y., and Kohsaka, S. (2000). Involvement of Iba1 in membrane ruffling and phagocytosis of macrophages/microglia. *J. Cell Sci.* 113, 3073–3084. doi: 10.1242/jcs.113.17.3073

Parakalan, R., Jiang, B., Nimmi, B., Janani, M., Jayapal, M., Lu, J., et al. (2012). Transcriptome analysis of amoeboid and ramified microglia isolated from the corpus callosum of rat brain. *BMC Neurosci.* 13:64. doi: 10.1186/1471-2202-13-64

Paxinos, G., and Franklin, K. (1998). *The mouse brain in stereotaxic coordinates.* San Diego, CA: Academic Press.

Penttinen, A., Parkkinen, I., Blom, S., Kopra, J., Andressoo, J., Pitkänen, K., et al. (2018). Implementation of deep neural networks to count dopamine neurons in substantia nigra. *Eur. J. Neurosci.* 48, 2354–2361. doi: 10.1111/ejn.14129

Plis, S. M., Hjelm, D. R., Salakhutdinov, R., Allen, E. A., Bockholt, H. J., Long, J. D., et al. (2014). Deep learning for neuroimaging: A validation study. *Front. Neurosci.* 8:229. doi: 10.3389/fnins.2014.00229

Rey, N. L., Steiner, J. A., Maroof, N., Luk, K. C., Madaj, Z., Trojanowski, J. Q., et al. (2016). Widespread transneuronal propagation of α-synucleinopathy triggered in olfactory bulb mimics prodromal Parkinson's disease. *J. Exp. Med.* 213, 1759–1778. doi: 10.1084/jem.20160368

Rua, R., Lee, J. Y., Silva, A. B., Swafford, I. S., Maric, D., Johnson, K. R., et al. (2019). Infection drives meningeal engraftment by inflammatory monocytes that impairs CNS immunity. *Nat. Immunol.* 20, 407–419. doi: 10.1038/s41590-019-0344-y

Schwabenland, M., Brück, W., Priller, J., Stadelmann, C., Lassmann, H., and Prinz, M. (2021). Analyzing microglial phenotypes across neuropathologies: A practical guide. *Acta Neuropathol.* 142, 923–936. doi: 10.1007/s00401-021-02370-8

Shi, F. J., Zhang, C. Y., and Qin, H. F. (2020). Is Iba-1 protein expression a sensitive marker for microglia activation in experimental diabetic retinopathy? *Int. J. Ophthalmol.* 14, 200–208. doi: 10.18240/ijo.2021.02.04

Volpicelli-Daley, L. A., Luk, K. C., and Lee, V. M. Y. (2014). Addition of exogenous α-synuclein preformed fibrils to primary neuronal cultures to seed recruitment of endogenous α-synuclein to Lewy body and Lewy neurite–like aggregates. *Nat. Protoc.* 9, 2135–2146. doi: 10.1038/nprot.2014.143

Walker, D. G., and Lue, L. F. (2015). Immune phenotypes of microglia in human neurodegenerative disease: Challenges to detecting microglial polarization in human brains. *Alzheimers Res. Ther.* 7:56. doi: 10.1186/s13195-015-0139-9

Welsh, R. M., and Seedhom, M. O. (2008). Lymphocytic choriomeningitis virus (LCMV): Propagation, quantitation, and storage. *Curr. Protoc. Microbiol.* 8, 15A.1.1–15A.1.11. doi: 10.1002/9780471729259.mc15a01s8

Whitelaw, N. C., Chong, S., Morgan, D. K., Nestor, C., Bruxner, T. J., Ashe, A., et al. (2010). Reduced levels of two modifiers of epigenetic gene silencing, Dnmt3a and Trim28, cause increased phenotypic noise. *Genome Biol.* 11:R111. doi: 10.1186/gb-2010-11-11-r111

York, E. M., LeDue, J. M., Bernier, L. P., and MacVicar, B. A. (2018). 3DMorph automatic analysis of microglial morphology in three dimensions from ex vivo and in vivo imaging. *eNeuro* 5:ENEURO.0266-18.2018. doi: 10.1523/ENEURO.0266-18.2018

Zhou, S., Halle, A., Kurt-Jones, E. A., Cerny, A. M., Porpiglia, E., Rogers, M., et al. (2008). Lymphocytic choriomeningitis virus (LCMV) infection of CNS glial cells results in TLR2-MyD88/Mal-dependent inflammatory responses. *J. Neuroimmunol.* 194, 70–82. doi: 10.1016/j.jneuroim.2007.11.018

Zusso, M., Methot, L., Lo, R., Greenhalgh, A. D., David, S., and Stifani, S. (2012). Regulation of postnatal forebrain amoeboid microglial cell proliferation and development by the transcription factor Runx1. *J. Neurosci.* 32, 11285–11298. doi: 10.1523/JNEUROSCI.6182-11.2012